Controls on the spatio-temporal patterns of induced seismicity in Groningen constrained by physics-based modeling with Ensemble-Smoother data assimilation

Thibault Candela[1], Maarten Pluymaekers[1], Jean-Paul Ampuero[2], Jan-Diederik van Wees[1,3], Loes Buijze[1], Brecht Wassing[1], Sander Osinga[1], Niels Grobbe[4], Annemarie G. Muntendam-Bos[4,5]

[1] TNO, Geological Survey of the Netherlands, Utrecht, The Netherlands
[2] Université Côte d'Azur, IRD, CNRS, Observatoire de la Côte d'Azur, Géoazur, Sophia Antipolis, France
[3] Utrecht University, department of geosciences, Utrecht, The Netherlands
[4] State Supervision of Mines, The Hague, The Netherlands
[5] Delft University of Technology, Department of Geoscience and Engineering, Delft, The Netherlands

---

PRE-PRINT WARNING

This manuscript has been submitted for publication in *Geophysical Journal International.* Subsequent versions of this manuscript may have different content. If accepted, the final version of this manuscript will be available via the *Peer-reviewed Publication DOI* link printed on this webpage.

Comments and questions are welcomed. Please contact the first author (Thibault Candela) via email (thibault.candela@tno.nl).

Abstract

The induced seismicity in the Groningen gas field, The Netherlands, presents contrasted spatio-temporal patterns between the central area and the south west area. Understanding the origin of this contrast requires a thorough assessment of two factors: (1) the stress development on the Groningen faults, and (2) the frictional response of the faults to induced stresses. Both factors have large uncertainties that must be honored and then reduced thanks to observational constraints. The present contribution builds upon the previous work of Candela et al. (2019), which was focused on the frictional response, and extends it by taking into account uncertainties in the stress development and by evaluating the relative effect of both factors. Ensembles of induced stress realizations are built by varying the Poisson's ratio in a poro-elastic model incorporating the 3D complexities of the geometries of the Groningen gas reservoir and its faults, and the historical pore pressure distribution. The a-priori uncertainties in the frictional response are mapped by varying the parameters of a seismicity model based on rate-and-state friction. The uncertainties of each component of this complex physics-based model are honored through an efficient data assimilation algorithm. By assimilating the seismicity data with an Ensemble-Smoother, the prior uncertainties of each model parameter are effectively reduced, and the posterior seismicity rate predictions are consistent with the observations. Our integrated workflow allows us to disentangle the contributions of the main two factors controlling the induced seismicity at Groningen, induced stress development and fault frictional response. Posterior distributions of the model parameters of each modelling component are contrasted between the central and south west area at Groningen. We find that, even after honoring the spatial heterogeneity in stress development across the Groningen gas field, the spatial variability of the observed induced seismicity rate still requires spatial heterogeneity in the fault frictional response. This work is enabled by the unprecedented deployment of an Ensemble-Smoother combined with physics-based modelling over a complex case of reservoir induced seismicity.

1. Introduction

Since the first earthquake recorded in the early 90's at the Groningen gas field, the situation has evolved dramatically with damage to over a thousand houses, culminating in an early phaseout of gas production. In parallel, various state-of-the-art workflows for probabilistic seismic risk assessment in the Groningen field have been developed (e.g. Bourne et al., 2014, 2017, 2018; Dempsey and Suckale, 2017), which were primarily designed to explain the observed rate of seismicity instead of in-depth understanding and unravelling of the relative contribution of each physical process at work. The induced seismicity rate in Groningen is potentially controlled by the combination of two processes: (1) the development of the induced stress changes on faults during gas production, (2) the frictional response of each fault when subjected to these induced stresses. In particular, depending on the fault frictional response, strong and fast stress changes might potentially lead to only low seismicity rates. Recently, Candela et al. (2019) proposed that spatio-temporal variabilities of the observed Groningen seismicity rate could be entirely explained by heterogeneities in the fault frictional response. However, spatial heterogeneities in elastic properties (as a consequence of the variations in the reservoir porosity (NAM, 2016) and indirectly revealed by subsidence inversion (Fokker and Van Thienen-Visser, 2016; Smith et al., 2019)), which can directly control the development of induced stress changes, were disregarded in their modelling approach.

The present contribution deploys a modelling strategy specifically designed to disentangle the relative importance between induced stress development and frictional response in controlling the induced seismicity at Groningen. To do so, a transparent modelling strategy is developed which allows to dissociate the contribution of each physical process.

When the objective is to disentangle the relative contribution of each physical process at work, intrinsically the modelling complexity increases as well as its computational demand and thus its run time on a standard PC. This calls for an efficient data assimilation procedure to reduce the number of models needed to appropriately constrain the posterior distribution of each model parameter for each physical process at work. Indeed, such complex and computationally heavier modelling strategy precludes the use of traditional brute-force or Markov Chain Monte Carlo (Foreman-Mackey et al., 2013) methods to screen the prior space of each model parameter. The present contribution develops an Ensemble-Smoother formulation with a single-step of data assimilation (Emerick and Reynolds, 2013a, b) which allows to constrain the posterior distributions of each model parameter with a relatively small ensemble of models. Combining both (i) a transparent physics-based modelling strategy honoring all the available a-priori knowledge and (ii) an efficient and robust data assimilation procedure, the causes of the spatio-temporal evolution of the seismicity at Groningen are effectively isolated and identified.

2. A transparent physics-based modelling strategy

The deployed modelling strategy is tailored to honor both: (i) the physics of the processes at work and (ii) all the pre-existing a-priori knowledge. The starting modelling ingredient is the flow simulation of the entire Groningen gas field, computed by the field operator, incorporating all the prior knowledge in terms of geology and subsurface hydrogeology, and history-matched with the subsidence observations (Bierman et al., 2015; Fokker and Van Thienen-Visser, 2016; Smith et al., 2019). The 3D numerical flow model for the full field contains approximately 650 000 cells, with an average cell size of 725x725 m and cell thickness of 5-10 m.

From this discretized pore pressure evolution, the second modelling step consists in computing the induced stresses at the Groningen faults. Following the same semi-numerical approach as Candela et al. (2019), and the so-called MACRIS method (Mechanical Analysis of Complex Reservoirs for Induced Seismicity, see van Wees et al., 2018, 2020), each cell of the flow grid is considered as a compacting nucleus of strain. The contribution of each of these nuclei is integrated to compute the poro-elastic stress changes along each fault of the Groningen field with a meter-scale spatial resolution. In order to account for the direct effect of the pore pressure on the effective normal stress at faults, the pore pressure at the faults is sampled from the fault compartments which have experienced the largest pressure changes. In a nutshell, MACRIS offers the unique opportunity to honor: (1) the heterogeneous spatio-temporal distribution of the pressure fields, (2) the fault geometry including its large-scale roughness and offset juxtaposing non-depleting rocks against the depleting reservoir, (3) the poro-elastic stress changes, (4) the direct pore pressure effect at faults. Combining both the poro-elastic and direct pore pressure effects, the modified Coulomb stress function can be calculated as:

$$S = \tau - [\mu - \alpha]\sigma_n' \quad (1)$$

where τ is the shear stress acting along the fault plane, σ_n' is the effective normal stress, μ the friction coefficient, and α is a constitutive parameter (zero in this study). MACRIS gives access to the stress changes along the 3D fault surfaces of the Groningen field. Because of the lack of constraint on the depth of the observed events, the seismicity catalog can be seen as a 2D field evolving over time. Consequently, for model-data comparison, the MACRIS output needs to be represented in 2D through time as well. There are a number of ways in which the up-scaling from 3 spatial dimensions to 2 spatial dimensions can be achieved. Following the approach and argumentation of Candela et al. (2019), we decide to represent each 3D fault pillar by its observation point recording the maximum Coulomb stressing rate.

From the induced stress changes at the fault, the seismicity rate can be computed incorporating the fault frictional response. Ignoring the fault frictional response, the traditional Coulomb failure model predicts that whenever the Coulomb stress reaches a threshold value, an earthquake is generated. This prediction is not in agreement with the observed seismicity, which generally shows a gradual decay following the onset of Coulomb stress decrease. Instead, the rate-and-state formalism reproduces the fact that the onset of frictional sliding is a non-instantaneous time-dependent process (as opposed to the instantaneity assumption of the Coulomb model), which introduces a time-dependent failure mechanism for the generation of earthquakes. Assuming a population of faults following a rate-and-state frictional behavior, and where the time-to-failure of the nucleation spots along the faults is uniformly distributed, Dieterich (1994) derived the following seismicity rate model:

$$R_D = \frac{r_0}{\theta \dot{S}_0} \quad \text{where} \quad \frac{d\theta}{dt} = \frac{1}{A\sigma_n'}\left[1 - \theta \frac{dS}{dt}\right] \tag{2}$$

and where R_D is the seismicity rate, θ is a state variable, S is the modified Coulomb stress function defined in equation (1). The constant r_0 is the steady-state background seismicity rate at the reference stressing rate $\dot{S}_0$. A is a dimensionless fault constitutive parameter.

Segall and Lu (2015) reformulated this seismicity rate equation to eliminate the state variable θ. They defined a normalized seismicity rate, relative to the background rate, as:

$$R = \frac{R_D}{r_0} \tag{3}.$$

The differential equation for R, derived from equations (2) and (3), is:

$$\frac{dR}{dt} = \frac{R}{t_a}\left[\frac{\dot{S}}{\dot{S}_0} - R\right] \tag{4}$$

where $t_a = A\sigma_n'/\dot{S}_0$ is the characteristic time delay for the earthquake nucleation process.

In summary, the physics-based modelling strategy involved two key steps: (1) computing the development of induced stress changes along the Groningen faults during reservoir production, (2) computing the seismicity rate taking as input the induced stress changes and honoring the fault frictional response. Both the induced stress development and the fault frictional response can control the spatio-temporal evolution of the seismicity rate at Groningen. In the sequel of the manuscript, the induced stress development refers to the MACRIS calculation, and the fault frictional response is embedded in Dieterich's seismicity rate theory.

Candela et al. (2019), instead of modeling the entire Groningen field, focused on two sub-areas: (i) the central area (C-area) where the seismicity rates are the highest and (ii) the south west area (SW-area) which has a much lower seismic activity (see Figure 1). They concluded that the difference in seismicity rate between these two sub-areas can be explained by a difference in the frictional response of the faults. This conclusion was based on the assumption of spatially homogeneous elastic properties when computing the poro-elastic stress changes. However, it is well-known that the porosity of the Groningen reservoir layer is spatially heterogeneous and can attests for the reservoir-scale heterogeneities in the uniaxial compaction coefficient (NAM, 2016), this last being linearly linked to the reservoir Young's modulus. Inversions of subsidence measurements have also highlighted the spatial heterogeneities in the compaction coefficient of the Groningen field (Bierman et al., 2015; Fokker and Van Thienen-Visser, 2016; Smith et al., 2019). In the present contribution, we test the hypothesis that the spatial heterogeneities in the Poisson's ratio can explain the difference in the seismicity history between the C-area and SW-area. Candela et al. (2019) assumed an identical Poisson's ratio of 0.2 for both areas of interest. However, using a lower Poisson's ratio for the C-area should lead to a much steeper stress path (defined as $\gamma = \frac{1-2\nu}{1-\nu}$, where ν is the Poisson's ratio, Buijze, 2020; Segall and Fitzgerald, 1998), and thus to relatively higher Coulomb stress rates. Assuming now that the frictional response of the Groningen faults is spatially uniform (that is, identical for both the C-area and the SW-area), these higher Coulomb stress rates might explain the earlier kick-off of the induced seismicity in the C-area relatively to the SW-area (see Figure 1).

With MACRIS the Poisson's ratio is involved at two levels in the calculation of the stress changes induced by the poro-elastic deformation of the reservoir (Figure 2). First, the Poisson's ratio scales the strength of the compacting sources (i.e. nuclei of strains), that is the compacting grid cells around the Groningen faults. Second, the same Poisson's ratio is used when the induced elastic strains along the Groningen faults are converted into induced elastic stresses by applying the generalized Hooke's law. Varying the Poisson's ratio in MACRIS, one can generate multiple stress solutions and thus test our hypothesis. To test the spatial heterogeneity in the Poisson's ratio, the two areas of interest, C-area and SW-area, are treated separately. The Poisson's ratio is kept spatially uniform at the scale of each area, but an ensemble of stress solutions is computed by varying the Poisson's ratio.

Figures 3 and 4 display the spatio-temporal evolution of the Coulomb stress changes along the Groningen faults of respectively the SW-area and C-area, assuming an identical Poisson's ratio of 0.2. The C-area presents a large number of faults with high Coulomb stress changes kicking off early in the history. Instead, in the SW-area, a single fault strand (oriented NW-SE) concentrates almost all the high Coulomb stress changes, and it is only late in the history that multiple faults start to experience high Coulomb stress changes. The contrast of fault orientation between both areas explains part of the difference in the spatio-temporal evolution of the Coulomb stress changes. Most of the faults of the C-area are optimally oriented; in contrast, the SW-area contains only one optimally-oriented NW-SE fault strand. Figure 5 quantitatively confirms this qualitative assessment by showing the cumulative distribution of the Coulomb stress rate for all the "fault patches" of both areas. A "fault patch" corresponds to the observation point where the stress changes have been computed. Note that the lengh-scale covered by each fault patch (that is, the distance between two pillars) is rougly constant for all the faults of the Groningen field. Overall the cumulative distributions

of Coulomb stress rate of fault patches of the C-area are much narrower than those of the SW-area. Three key observations can be drawn. First, the C-area contains a higher fault density underlined by a higher total number of fault patches. Second, the C-area presents a higher number of fault patches experiencing average to high Coulomb stress rates (between 0 and 0.2 MPa/year). Third, the SW-area displays a higher number of fault patches experiencing very high Coulomb stress rates (> 0.35 MPa/year). To summarize, the C-area is characterized by a higher density of fault patches with an average to high Coulomb stress rate kicking off early in the history. Instead, the SW-area is characterized by a lower density of fault patches, with a relatively large number of them experiencing very high Coulomb stress rates at a late stage during the field history.

Focusing on the C-area and now assuming an uniform but relatively small Poisson's ratio of 0.05, Figure 6 and Figure 7 indicate, respectively, the spatio-temporal evolution of the Coulomb stress changes and the cumulative distribution of the Coulomb stress rates. As expected, for each timestep, both the magnitude of stress changes and the number of fault patches experiencing high Coulomb stress rates are larger than in the previous scenarios with a Poisson's ratio of 0.2.

3. Ensemble-Smoother for seismicity data

The objective is now to develop an efficient data assimilation scheme in order to find the optimum set of posterior model parameters that give the best agreement between the spatio-temporal evolution of the observed seismicity rate and the computed rate.

Before describing the details of the data assimilation procedure, it is important to define the earthquake catalogue used as data. This earthquake catalogue has been compiled by the Royal Netherlands Meteorological Institute (KNMI). KNMI has monitored seismicity in the Netherlands since at least 1986. From the dedicated borehole network deployed since 1995 by KNMI and constantly upgraded over the years, the earthquake detection capability improved: the magnitude of completeness kept decreasing from 1.5 in 1995 to around 0.5 today. For sake of direct comparison of our results with the ones of Candela et al. (2019), we restrict our analysis to all events with $M_L \geq 1.0$. As mentioned previously, constrained by the large uncertainty attached to the depth of each observed event, the seismicity catalogue is considered as a 2D field.

In order to compare the computed 2D seismicity rates to the observed ones, both uncertainties in model (e.g., pore pressure distribution, fault orientation, stress calculation) and data (e.g., earthquake location) should be accounted for. We applied a Gaussian smoothing to the seismicity rate R_D fields to incorporate uncertainties. In order to compute the smoothed seismicity rate fields, $\overline{R_D}$, for each R_D field, the following integration over space is performed:

$$\overline{R_D}(x,y) = \iint_{-\infty}^{+\infty} R_D(x-x', y-y')\, G(x',y')\, dx'dy' \qquad (5),$$

where Gaussian operator is defined as:

$$G(x,y|\sigma_s) = \frac{1}{2\pi\sigma_s^2} e^{-\frac{x^2+y^2}{2\sigma_s^2}} \qquad (6).$$

As a result, the five model parameters to be optimized are: (1) the Poisson's ratio used in the computation of the stress development with MACRIS, (2) the three parameters $[A, r_0, \dot{S}_0]$ of the

Dieterich's seismicity rate theory governing the fault frictional response, and the characteristic length scale (standard deviation) of the Gaussian smoothing σ_s.

It is important to note here that MACRIS is probably the only modelling approach that resolves 3-D poro-elastic stress changes along multiple faults with a meter-scale spatial resolution while honoring the full details of the reservoir and fault geometries. Finite-element numerical computations could achieve this only through a tremendous meshing effort and running time. Here, it takes 5 hours on a standard PC for MACRIS to compute the depletion-induced stress changes along the 76 faults of the C-area with a meter-scale spatial resolution. Even if such achievement is exceptional, this run time is still not adapted for a traditional data assimilation scheme such as brute-force grid search or the Markov Chain Monte Carlo algorithm. A much more efficient data assimilation procedure, with a low number of forward simulations, needs to be developed for a robust calibration of model parameters.

An ensemble-based approach is deployed to update the prior model ensembles with the use of the data. The Ensemble Kalman Filter has proven to be very effective in weather forecasting, but also in reservoir engineering approaches (Evensen, 2009). Every time that new data are collected, the Ensemble Kalman Filter procedure is applied, and the model parameters and predictions are updated. A progressively developing forecast mean and bandwidth is created. Another alternative, often used for subsidence inversion (Fokker et al., 2012, 2016; Baù et al., 2015), is to use an Ensemble-Smoother where the new posterior ensemble is constructed in a single step (van Leeuwen and Evensen, 1996). This is the data assimilation procedure deployed here for the first time over a complex case with real seismicity data. However, one outstanding challenge is the discrete nature of the seismic events. Indeed, ensemble-based approaches, both Ensemble Kalman Filter and Ensemble-Smoother, are designed for assimilating continuous data. As developed by Tarrahi and Jafarpour (2012) and Tarrahi et al. (2015) for the Ensemble Kalman Filter and for synthetic scenarios and data, a Gaussian smoothing is applied here to the real discrete seismicity data before applying the Ensemble-Smoother in the same fashion as defined in equations (5) and (6). Thus two distinct Gaussian kernels are applied here. The first one σ_s to smooth the model outcomes and honor model uncertainties, and as mentioned previously considered as a model parameter to be optimized during the data assimilation step. The second Gaussian kernel must be applied to the seismicity data where the standard deviation of the kernel is fixed and is intended to map the uncertainty in event locations. Note here that, in practice, this approach would allow to handle: (1) different uncertainties for each event location, and (2) different uncertainties between x and y directions. In this study, a unique, isotropic Gaussian kernel is selected.

The Ensemble-Smoother approach consists of an inversion scheme, for which the goal is to maximize an objective function of the form (Menke, 1989; Tarantola, 2005):

$$J(m) = exp[-\frac{1}{2}((G(m) - d)^T\, C_d^{-1}\, (G(m) - d) + (m - m_0)^T\, C_m^{-1}\, (m - m_0))] \qquad (7),$$

where m and $G(m)$ are respectively the optimized (posterior) vector of model parameters $[\nu, A, r_0, \dot{S}_0, \sigma_s]$ and model predictions. Following this approach, the objective function is integrated in an inversion scheme seeking the solution for the vector m of model parameters that optimize the match with data d and with prior information m_0. The Ensemble-Smoother explicitly includes our prior knowledge m_0 and the model covariance matrix C_m (explained in the sequel of this section) with the term $(m - m_0)^T\, C_m^{-1}\, (m - m_0)$.

The optimal "least-square" solution for one particular realization, assuming a linear inverse problem, is given by:

$$\widehat{m} = m_0 + C_m G^T (G C_m G^T + C_d)^{-1} (d - G m_0) \quad (8).$$

For an ensemble-based estimate with a non-linear problem we define GM_0 as the result of the non-linear forward model working on all the members of the ensemble, that is the ensemble of prior event density predictions covering the time window of interest. For an ensemble-based estimate, the Ensemble-Smoother then gives as updated model parameter ensemble:

$$\widehat{M} = M_0 + M_0' \{[GM_0']^T C_d^{-1} GM_0' + (N_e - 1) I\}^{-1} \times [GM_0']^T C_d^{-1} (D - GM_0) \quad (9)$$

Equation (9) uses the expression for the empirically estimated model covariance matrix $C_M = M_0' M_0'^T / (N_e - 1)$ for the ensemble of model realizations (N_e is the number of members of the ensemble). The estimate for C_M includes the known and belief bandwidths of the model parameters. Primes in equation (9) indicate anomalies with respect to the ensemble mean as M_0' = M_0 − <M_0>. Finally $D = (d + \varepsilon_1, d + \varepsilon_2, \ldots d + \varepsilon_{N_e})$ corresponds to an ensemble of seismic event density data realizations created adding to the vector data d different random noise vectors ε that lie within the data uncertainty range. Following Tarrahi and Jafarpour (2012), the error of the event density data is considered as proportional to the value of the event density data and the variance at the kth grid block of the event density data ρ is computed as:

$$\sigma_k^2 = \left(\sigma_{min} + \frac{(\sigma_{max} - \sigma_{min})(\rho^k - \rho_{min})}{(y_{max} - y_{min})}\right)^2, k = 1,2, \ldots, N_d \quad (10),$$

where σ_{max} and σ_{min} are respectively the minimum and maximum variances specified for the observed event density. The member j of the perturbed observed event density at location k, can then be written as:

$$\rho_k^j = \rho_k + \varepsilon_k^j, j = 1, 2, \ldots, N_e \quad (11),$$

$$\varepsilon_k^j \sim N(0, \sigma_k^2) \quad (12).$$

Two ensembles of forward simulations thus need to be run, the prior ensemble with the prior ensemble of model parameters M_0, and the posterior ensemble with the updated posterior ensemble of model parameters $\widehat{M}$. A simple sensitivity analysis revealed that once the size of the prior ensemble is as large as 100-200 members, $\widehat{M}$ is stable. Thus the total number of forward simulations can be kept as low to 100-200 (prior + posterior) in order to obtain a robust model conditioning. This is an excellent achievement considering that with traditional estimation algorithms (e.g. brute-force grid search or the Markov Chain Monte Carlo algorithm), several thousands of simulations would be required for a proper coverage of the prior model parameter space.

4. Full Groningen field with one single stress scenario

Before running prior ensembles of MACRIS stress realizations varying the Poisson's ratio for both the C-area and SW-area (covered in the next Section 5), the full Groningen field is considered with a single MACRIS stress realization computed with a fixed Poisson's ratio of 0.2. In other words, we seek to optimize, for the time window from 1 January 1993 to 31 December 2017 [1993-2018],

solely 4 model parameters: the three parameters $[A, r_0, \dot{S}_0]$ of Dieterich's seismicity rate theory governing the fault frictional response, and the standard deviation of the Gaussian smoothing σ_s.

Posterior ranges of model parameters (Figure 8) for the full Groningen field are similar to the ones derived by Candela et al. (2019) for the C-area (see Table 1). More specifically, for the full Groningen field and considering an average effective normal stress of 12.5 MPa (derived from MACRIS) the mean characteristic relaxation time of seismicity ($t_a = A\sigma_n'/\dot{S}_0$) is 108 years. In Candela et al. (2019), for the C-area t_a was estimated to be 87 years and for the SW-area to be 6700 years. The similarity between the t_a derived from the whole Groningen field and the t_a derived for the C-area is not surprising: because most of the induced events are located in the C-area, during the data assimilation step, the C-area dominates the update-procedure of the spatially uniform sets of model parameters of the full Groningen field.

The temporal evolution of the mean posterior event rate for the full Groningen field closely follows the one of the data (see Figure 9). This match is solely controlled by the update of the three parameters $[A, r_0, \dot{S}_0]$ modulating the fault frictional response. Indeed, the update of the Gaussian smoother σ_s solely controls the spatial pattern. Consequently, since the calibration of the model parameters is dominated by the C-area, where most of the data-events are located, a significant residue is observed between the spatial patterns of event density of the mean posterior and the data (Figure 10). The temporal event rate is nothing more than the spatial integration of the event density. Thus in order to match the spatial pattern of the data event density, the mean posterior model over-estimates the event density at the locations (including the SW-area) surrounding the C-area, and it under-estimates the event density in the C-area.

To conclude for the full Groningen exercise, the Ensemble-Smoother performs well, although the spatial pattern of event density of the posterior clearly diverges from that of the data. This mismatch must be attributed to our forward modelling strategy, which is certainly missing complexities when the model parameters of both the induced stress development and the fault frictional response are assumed spatially uniform.

5. Dual contribution of stress development and frictional response

Varying the Poisson's ratio, two separate prior ensembles of MACRIS stress realizations are now computed for both the C-area and SW-area. For the sake of comparison with the results obtained by Candela et al. (2019), the calibration time window is now from 1st January 1993 to 31 December 2015 [1993-2016]. We seek to optimize both the parameters controlling the stress development and the ones controlling the fault frictional response (that is, the Dieterich's model parameters).

The resulting posterior distributions of the frictional parameters $[A, r_0, \dot{S}_0]$ (including the Gaussian smoother σ_s) are significantly different for both areas of interest (Figure 11). Considering an average effective normal stress of 10 MPa and 12.5 MPa (both derived from MACRIS) for respectively the C-area and SW-area, the mean characteristic relaxation times of seismicity are 90 years and 5470 years, respectively.

The posterior distributions of the Poisson's ratio (Figure 12 and Table 1) are also significantly different for both areas of interest. The mean posterior of the SW-area is very close to the a-priori

constant value of 0.2 used in Candela et al. (2019). Instead, the inverted mean posterior Poisson's ratio of the C-area is very low, close to 0.015.

For both areas of interest, the posterior ensembles of event rates (Figure 13) follow very closely the long-period fluctuations of the observations. In both cases, the range of variability of the posteriors is sufficiently large, demonstrating that the collapse of the posterior ensembles towards one unique solution has been prevented (Emerick and Reynolds, 2013a). This is particularly interesting considering that a rather drastic update procedure of both prior ensembles were imposed since only one step of data assimilation has been performed. Following a more progressive update procedure applying multiple steps of data assimilation is apparently not warranted in our case. The larger variance of the posterior ensemble event rate of the SW-area is a direct consequence of the relatively broader posterior distributions of its model parameters.

Compared to the full Groningen inversion (Figure 10), the spatial patterns of the posterior event densities have clearly improved for both areas of interest (Figure 14). This is especially the case for the C-area where now the posterior event density does not under-estimate the observed event density over the entire surface area anymore.

Figure 15 demonstrates that the difference in the posterior model parameters between the C-area and SW-area has a significant impact on the modelled cumulative number of events. Using the mean posterior model parameters of the SW-area for the C-area, the cumulative number of events is significantly lower than both (i) the observations at the C-area and (ii) the modelled cumulative number of events for the C-area using the mean posterior model parameters of the C-area.

6. Resolution of the Poisson's ratio

Can our inversion procedure effectively constrain the Poisson's ratio? Can we demonstrate that a seismicity history cannot be equally explained by two different Poisson's ratios even after tuning the Dieterich's model parameters? Our objective here is to assess if our inversion procedure can discriminate two models computed with two different Poisson's ratios. A corollary is: can we estimate why our results indicate that a model with a lower Poisson's ratio can better explain the C-area seismicity rate history? We address these questions for the C-area by comparing the quality-of-fit of the data by the optimum model obtained in this study and the one derived for a Poisson's ratio of 0.2 by Candela et al. (2019). We use two metrics to assess the quality-of-fit. Our first metric is the $RMSE$, defined as the root-mean-square of the residuals between data and the optimum model:

$$RMSE = \sqrt{\frac{\sum_{i=1}^{i=N_d} (\boldsymbol{d} - \boldsymbol{G}(\hat{\boldsymbol{m}}))^2}{N_d}} \qquad (13),$$

where N_d is the number of observations. Our second metric is the χ^2 method, which judges if the average of the squared residuals is of the order of the sum of the covariances of the data and model. The normalized $\frac{\chi^2}{N_d}$ reads:

$$\frac{\chi^2}{N_d} = \frac{1}{N_d} (d - G(\hat{m}))^T \left[C_d + C_{G(\hat{m})}\right]^T (d - G(\hat{m})) \qquad (14),$$

where C_d and $C_{G(\hat{m})}$ are respectively the covariances of data and model. Lower values of RMSE indicate a better fit. A $\frac{\chi^2}{N_d}$ close to unity means that the model matches the data at a level consistent with the error covariance of the data. For the C-area, both metrics indicate a better fit of the model derived here ($RMSE$ = 5.4, $\frac{\chi^2}{N_d}$ = 0.8) than of the one derived in Candela et al. (2019) ($RMSE$ = 7.9, $\frac{\chi^2}{N_d}$ = 2.8). Our inversion procedure can thus effectively discriminate predictions with two different Poisson's ratios, and using a lower Poisson's ratio for the C-area leads to a better match of the observations.

To dive deeper into this question of the resolution of the Poisson's ratio, it is beneficial to use a synthetic "ideal" case for the analytical solution of the along-fault stress development during the depletion history. We pursue this in the remainder of this section, to gain confidence in the results obtained by our inversion procedure.

Re-writing equations (3) and (4) in dimensional form it reads:

$$\dot{S} = (A\sigma_n')\frac{\dot{R}_D}{R_D} + \left(\frac{\dot{S}_0}{r_0}\right)R_D \qquad (15).$$

Equation (15) tells us that the same seismicity history can be fitted by another Coulomb stressing rate history of different amplitude but same time-dependence (i.e. x times the original $\dot{S}$) by adjusting the Dieterich's model parameters $A\sigma_n'$ and $\frac{\dot{S}_0}{r_0}$ (multiplying both by the constant x). In other words, if varying the Poisson's ratio would solely modify the amplitude of the Coulomb stressing rate, the observed seismicity rate history could be equally fitted/explained by multiple Poisson's ratio after adjusting the Dieterich's model parameters $A\sigma_n'$ and $\frac{\dot{S}_0}{r_0}$. Therefore, our inversion procedure would not help to constrain the Poisson's ratio. However, this conclusion only holds if changing the Poisson's ratio only modifies the amplitude of the Coulomb stressing rate but not its shape (i.e., $\dot{S}_0$ normalized by its max value), which is only fulfilled when the friction μ is kept constant in the calculation of the Coulomb stressing rate defined as:

$$\dot{S} = \dot{\tau} - [\mu - \alpha]\dot{\sigma_n'} \qquad (16).$$

In our case, as implemented by Rubin and Ampuero (2007), the changes in the friction (defined as $\mu = \tau/\sigma_n'$) during the induced stressing history (that is the depletion history in our case) are honored. Therefore, when the Poisson's ratio varies, both the amplitude and the time-dependent shape of the Coulomb stressing rate are modified. This can be demonstrated by considering the analytical solution for a laterally extensive depleting reservoir undergoing uniaxial compaction (e.g. Fjaer et al., 2008) where the changes in effective normal stress and shear stress induced by a depletion history $\Delta P(t)$ are respectively:

$$\Delta\sigma_n'(t) = [0.5\gamma\,(1 + \cos(2\varphi)) - 1]\,\Delta P(t) \qquad (17),$$

and

$$\Delta\tau(t) = [-0.5\gamma\,\sin(2\varphi)]\,\Delta P(t) \qquad (18).$$

In equations (17) and (18), γ is the stress path defined previously as $\gamma = \frac{1-2\nu}{1-\nu}$; and $\varphi = 90 - fault\ dip$. Assuming initial conditions as $\tau_{init} = 5\ MPa$ and $\sigma_{init} = 13\ MPa$, and a depletion history representative of the Groningen gas field, Figure 16 presents the Coulomb stressing rate

histories and effective normal stress histories considering two different Poisson's ratios. $A\sigma_n'$ in equation (10) cannot be interpreted as a constant, since in our approach the temporal changes in effective normal stress are honored when solving the ordinary differential equation (4). Modifying the Poisson's ratio affects thus substantially the shape of both the Coulomb stressing rate history and the effective normal stress history (see Figure 16). Our inversion procedure should thus effectively constrain the Poisson's ratio since an observed seismicity rate history can only be reproduced by one unique modelled seismicity rate history generated by one unique Poisson's ratio. In other words, a seismicity rate history obtained with one stressing history (that is generated by one Poissson's ratio) cannot be reproduced by a different Poisson's ratio adjusting the Dieterich's parameters.

To discuss the resolution of the Poisson's ratio, one can rearrange equation (15) as:

$$aX(t,\nu) + bY(t,\nu) = 1 \quad (19),$$

where, for a given Poisson's ratio ν value, $X = \sigma_n'\dot{R}_D/\dot{S}R_D$ and $Y = R/\dot{S}$ are known time series, and $a = A$ and $b = \frac{\dot{S}_0}{r_0}$ are the unknown Dieterich's model parameters. For each given Poisson's ratio ν, the optimal values of a and b can be readily obtained by standard least-squares regression of equation (19). The objective function is defined as:

$$J(m) = \|G(m) - d\|^2 \quad (20)$$

where $m = [a, b]$, G is a matrix $[X, Y]$ and d is a vector of ones $[1]$. The least-squares solution is:

$$\hat{m} = (G^T G)^{-1} G^T d \quad (21).$$

To account for the covariances of X and Y, an orthogonal regression solver can be employed. X and Y are combinations of model predictions (σ_n' and $\dot{S}$) and data ($\dot{R}_D$ and R_D). In order to identify the resolution of the Poisson's ratio, one can consider, as previously for Figure 16, the analytical solution for the development of stresses (see equations (17) and (18)) induced along a fault embedded in a laterally extensive depleting reservoir undergoing uniaxial compaction. X and Y are combinations of model predictions (σ_n' and $\dot{S}$) and data ($\dot{R}_D$ and R_D). In our analytical example, the data ($\dot{R}_D$ and R_D) are generated with a known set of parameters: $\nu = 0.05$, $a = 0.22$, and $b = 0.31$. Note that the Dieterich's model parameters are similar to the inverted mean optimums for the C-area, and the Poisson's ratio of 0.05 is considered as representative of the low inverted mean optimum value of 0.015 for the C-area (see Table 1). For each member of the prior range of Poisson's ratio, the least-squares regression problem is solved and both the optimal values of a and b, and the two metrics for the quality-of-fit (equations (13) and (14)) are obtained. Figure 17 demonstrates that, according to both metrics, the best model is effectively the one computed with a Poisson's ratio of 0.05 as the one of the data. In addition, the minimum values of both metrics (that is the best model) is rather sharp and well defined, meaning that small deviations from the optimum Poisson's ratio of 0.05 already result in suboptimal match between model and data. This last observation demonstrates that the Poisson's ratio can be well resolved following our inversion procedure. In other words, the seismicity history of the data can only be explained by one unique Poisson's ratio.

Figure 18 indicates that suboptimal models generated with Poisson's ratios higher than the one used for the data (that is, 0.05), are characterized by lower Dieterich model parameters a and b relatively to the ones used for the data (that is respectively 0.22 and 0.31). This same trend derived for the

synthetic analytical case is also observed using MACRIS and the real seismicity catalog. The optimum Dieterich's parameters a and b derived in this study with the optimum Poisson's ratio of 0.015 are higher relatively to the ones obtained by Candela et al. (2019) where a fixed Poisson's ratio of 0.2 was used (see Table 1).

Our analytical exercise can be considered as representative of the behavior of each fault patch constituting the C-area. Since the modelled seismicity rate for the C-area results from the integration of the local seismicity rate for each fault patch, one can also expect the Poisson's ratio to be well resolved for the real case C-area as indicated by the posterior distribution of the Ensemble-Smoother procedure (Figure 12). Both the performance metrics ($RMSE$ and $\frac{\chi^2}{N_d}$) of the real case and our analytical exercise, reveal that the Poisson's ratio (controlling the stress development during the Groningen depletion history) and the Dieterich's model parameters (controlling the frictional response of the Groningen faults) can be well constrained.

7. Concluding discussion

7.1. "Apparent" background stressing and seismicity rates

Our assimilation procedure of observed events started in 1993 when a significant earthquake activity started to be recorded. Consequently, Dieterich's seismicity rate equation (4) was solved assuming an initial condition at steady state, that is $R(0) = 1$ in 1993. However, the start of the human-induced perturbation of the Groningen field goes back to 1968, and hence it is most likely that the background activity was not at steady state in 1993. The background stressing rate and seismicity rate inferred for 1993 should not be interpreted as real steady state background values (before the start of human-induced perturbations by gas production), but should be understood as "apparent background values", which are actually the reference values at the initial time of the analysis, here 1993. Starting our analysis in 1993 and applying Dieterich's theory, we made the intrinsic assumption that the Groningen faults were one stress drop from failure, that is critically stressed at this time. Other alternative strategies could have been deployed to start the analysis at the onset of gas production in 1968 and to honor the fact that the Groningen faults were probably far from failure at this time. Either an additional degree of freedom as an activation threshold could have been implemented (Zhai et al., 2019), or Dieterich's equation could have been reformulated to explicitly handle the Groningen dormant faults (Heimisson et al., 2020).

7.2. Potential missing modelling ingredients for the stress development

It remains to understand why our inversion procedure favors such very low mean posterior Poisson's ratio (0.015) for the C-area. For a lower Poisson's ratio, the seismicity data requires a higher stressing rate. One missing ingredient that could lead to higher stressing rates without the need of a very low Poisson's ratio is the elastic stress transfers between induced events. Instead of tackling the difficult challenge of explicitly modelling the additional stress changes induced by each rupture event, we here focus on the statistical removal from the observed catalogue of the events triggered by these stress transfers. Candela et al. (2019; Appendix A.3) applied the declustering procedure

developed by Zaliapin and co-workers (Zaliapin et al. 2008, Zaliapin and Ben-Zion 2013, Zaliapin and Ben-Zion 2016) for both the C-area and SW-area. Interestingly, the declustering analysis of Candela et al. (2019; Appendix A.3) indicates that the C-area is more prone to earthquake triggering compared to the SW-area: the aftershock proportion is 15% for the C-area and only 4% for the SW-area. The relatively higher percentage of triggered aftershocks might explain why only the C-area is characterized by a very low mean posterior Poisson's ratio. This hypothesis can be further tested by comparing the modelled event rate of the C-area using a Poisson's ratio of 0.2 against the declustered catalogue (see Figure 19). As expected, using a Poisson's ratio of 0.2, the modelled cumulative number of events is significantly lower relatively to the one derived using the mean optimum inverted value of 0.015. More importantly, using a Poisson's ratio of 0.2, the modelled cumulative number of events is lower than the cumulative number of mainshocks of the declustered catalogue. Using a Poisson's ratio somewhere in between 0.015 and 0.2, the model should thus closely explain the declustered catalogue. The difference in optimum Poisson's ratio between the C-area and SW-area should thus persist even after accounting for the elastic stress transfers.

An additional missing modelling ingredient is the plastic compaction of the reservoir. Indeed, recent laboratory experiments on core samples of the Groningen reservoir rock show that a large part (up to 50%) of the deformation occurring during laboratory-simulated depletion is inelastic (Hol et al., 2015; Hol et al., 2018; Pijnenburg et al., 2018; Pijnenburg et al., 2019). Can the relatively lower optimum Poisson's ratio of the C-area compared to the one of the SW-area be explained by plastic compaction? In other words, can the higher propensity to plastic compaction of the C-area explain its apparently lower Poisson's ratio? Multiple factors can potentially control the relative proportion between elastic and plastic deformation, e.g. rock porosity, clay content, initial mean effective stress directly linked to the reservoir depth (Buijze, 2020). These factors are contrasted between the C-area and SW-area; e.g. rock porosity and reservoir depth are both higher for the C-area. Interestingly Buijze (2020) indicates that the primary response of the Groningen stress path can be approximated with a linear elastic behavior. In other words, using an apparent Poisson's ratio, the laboratory-observed elasto-plastic stress path of the Groningen reservoir rocks can be mimicked. One can thus postulate that the difference in optimum Poisson's ratio between both areas of interest could be an apparent result of a difference in the relative proportion of elastic and plastic deformation.

Another elastic parameter which could have been considered in addition to the Poisson's ratio is the Young's modulus. However, the MACRIS calculation, as well as any poro-elastic solutions honoring the fault offsets and depletion heterogeneities, would lead to an identical stress path and thus Coulomb stress rate history when varying the Young's modulus (Fjaer et al., 2008; van Wees et al., 2018). Indeed, when elastic properties are considered identical between the reservoir and its surrounding, varying the Young's modulus has no effect on the stress path. However, upgrading the current MACRIS calculation in order to handle the potential contrast in Young's modulus between the reservoir and its surrounding, would lead to different stress paths. This is what van Wees et al. (2018) demonstrated for the Groningen gas field using a numerical Finite-Element approach. Indeed, Figure 4 of van Wees et al. (2018) demonstrates that for a typical Groningen fault, the Coulomb stress rate should be 25-30% higher for the C-area relatively to the SW-area when honoring the contrast in Young's modulus between reservoir and its surroundings while keeping constant the Poisson's ratio. This is a direct consequence of the higher difference in Young's modulus at the C-area between the reservoir layer and its surroundings. The well-documented relatively higher porosity of the reservoir layer at the C-area is at the origin of its low Young's modulus (NAM, 2016);

this last directly explains the higher contrast in Young's modulus between the reservoir and its surroundings. Interestingly, the Coulomb stress rate amplification of 25-30% found in the simulations of van Wees et al. (2018) is in agreement with the difference in Poisson's ratio that our inversion highlights between the C-area and SW-area. Two independent modelling strategies, one honoring the effect of the contrast in Young's modulus between the reservoir and its surrounding (van Wees et al., 2018), and our approach honoring the Poisson's ratio effect, thus point toward the same direction of a relatively higher Coulomb stress rate for the C-area.

7.3. Concluding remarks

One key advantage of our forward modelling strategy (coupling MACRIS with Dieterich's seismicity rate theory) is that the effect on the seismicity predictions of each modelling component (stress development and frictional response) can be individualized and thus tracked down. Indeed, our prime achievement is the disentanglement of the relative contributions of each physical process controlling the occurrence of induced seismicity at the Groningen gas field. Without deploying an efficient Ensemble-Smoother formulation, which only requires a small prior ensemble to constrain the posterior distribution of each model parameter, this disentangling exercise would not be feasible.

Our integrated workflow (coupling a physics-based forward modelling and an efficient data assimilation procedure) demonstrates that even after honoring the potential spatial heterogeneity in stress development (i.e. Poisson's ratio) across the Groningen gas field, the spatial variability of the observed induced seismicity at Groningen requires spatial heterogeneity in fault frictional responses (i.e. Dieterich's model parameters). A corollary is that any modelling strategy seeking to predict seismicity in the Groningen field must explicitly honor spatial heterogeneities in both (1) stress development and (2) fault frictional response.

	This work			Candela et al. (2019)	
	Full Groningen	**C-area**	**SW-area**	**C-area**	**SW-area**
A	0.13	0.22	0.35	0.14	0.8
$\dot{S}_0$ (MPa/Year)	0.015	0.025	0.0008	0.02	0.0015
r_0 (event/Year)	0.27	0.35	0.07	0.4	0.075
σ_s (m)	1750	1750	2500	1700	2750
ν	0.2 (constant)	0.015	0.2	0.2 (constant)	0.2 (constant)

Table 1 Comparison of the mean posterior model parameters of this study and the ones derived in Candela et al. (2019).

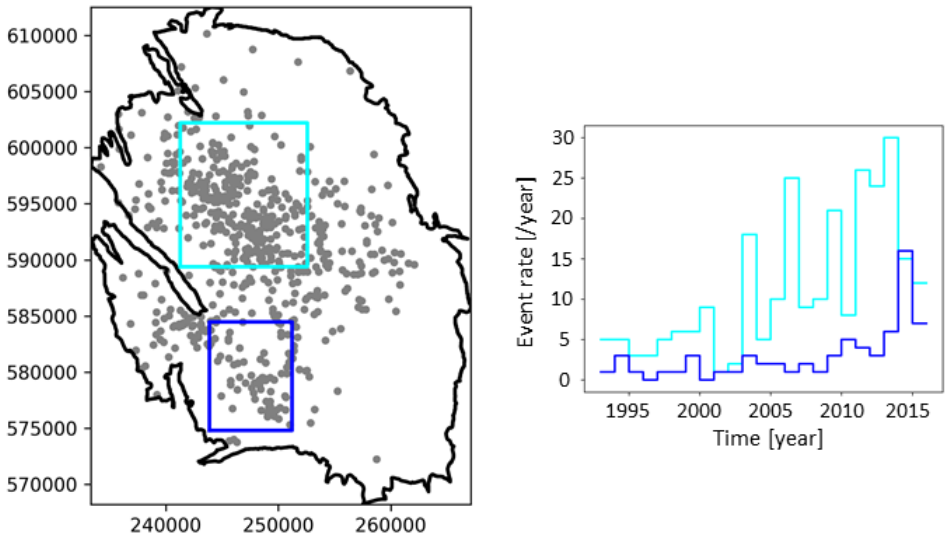

Figure 1 Contrast in the spatio-temporal seismicity dynamics at the Groningen gas field (modified from Candela et al., 2019). Left: Location of the two selected sub-areas (cyan: C-area, blue: SW-area) inside the Groningen gas field (black contour); the grey dots indicate the locations/hypocenters of the observed induced events with a minimum magnitude of 1.0. Right: Observed yearly event rates with a minimum magnitude of 1.0.

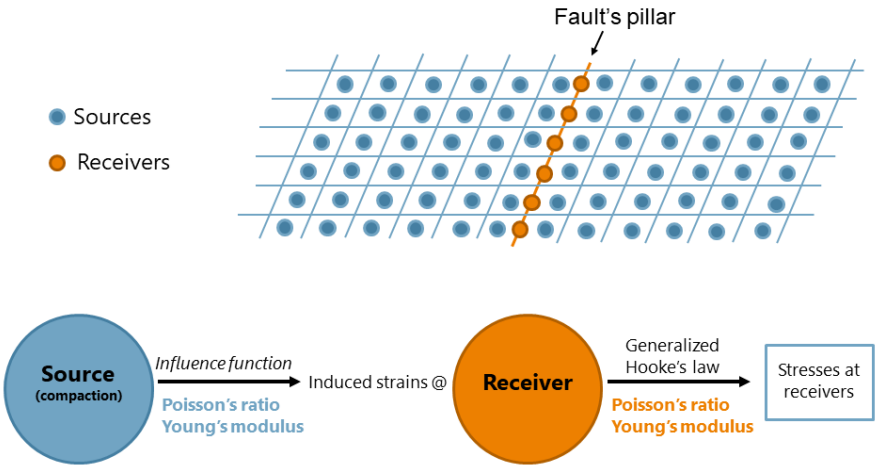

Figure 2 Schematics of the use of the elastic properties in MACRIS.

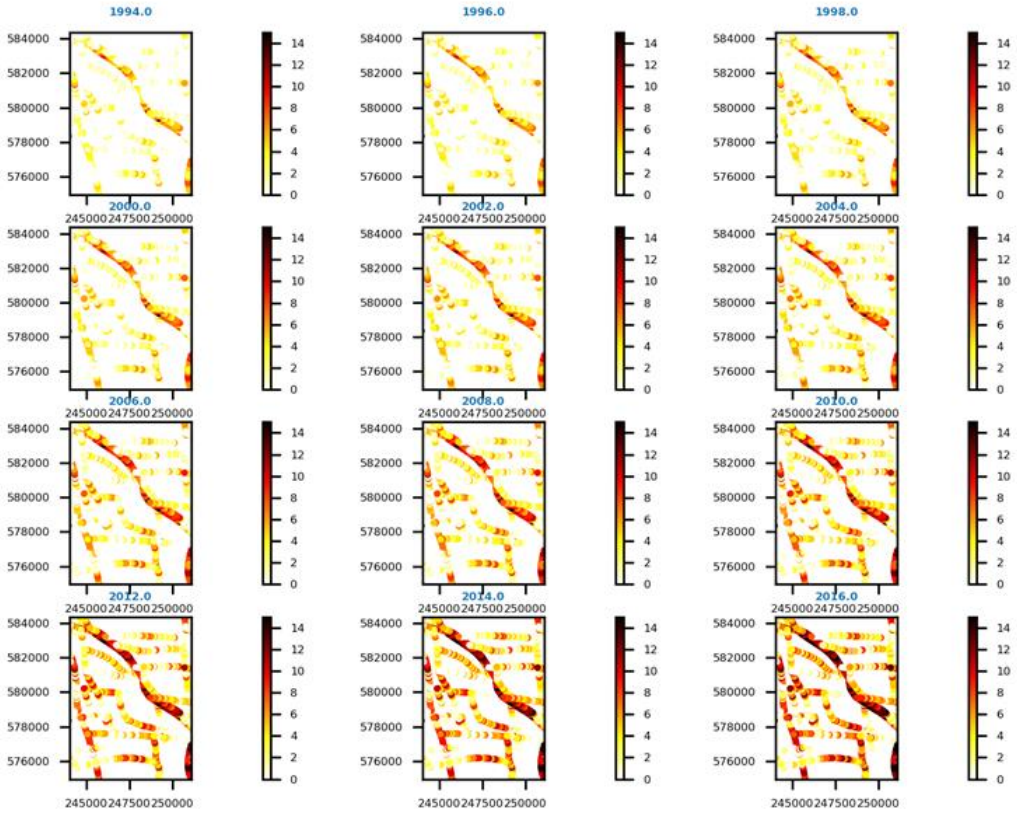

Figure 3 Spatio-temporal evolution of the Coulomb stress changes (MPa) for the SW-area using a Poisson's ratio of 0.2.

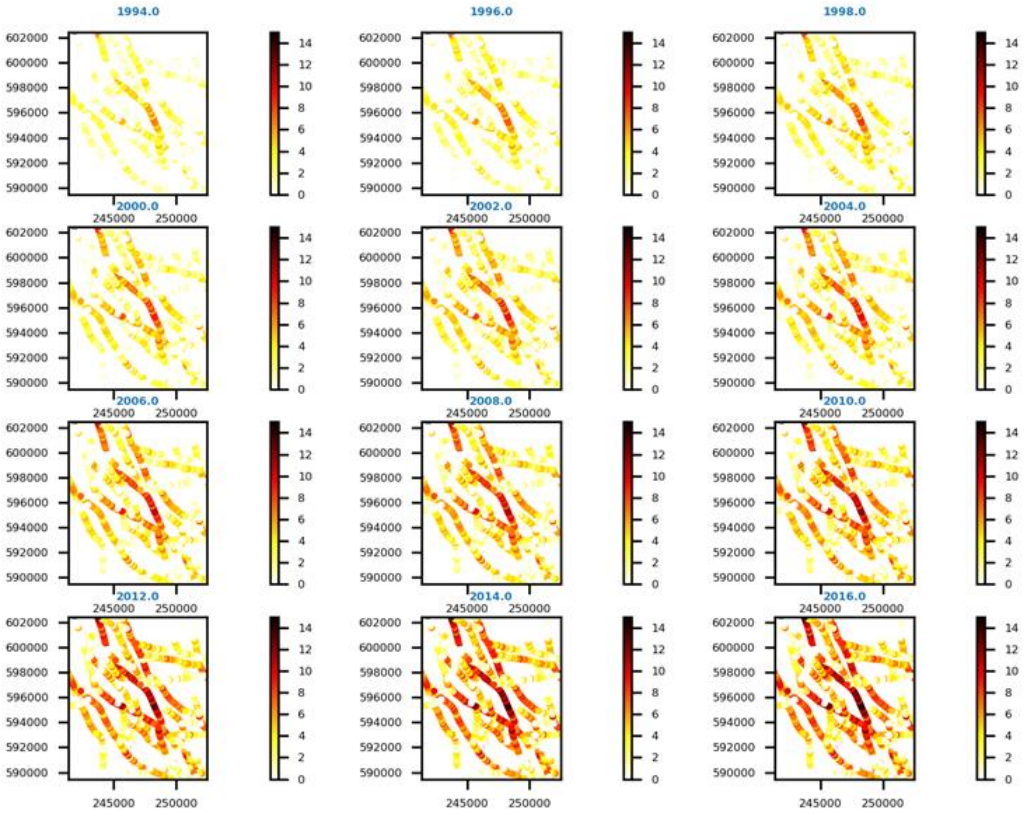

Figure 4 Spatio-temporal evolution of the Coulomb stress changes (MPa) for the C-area using a Poisson's ratio of 0.2.

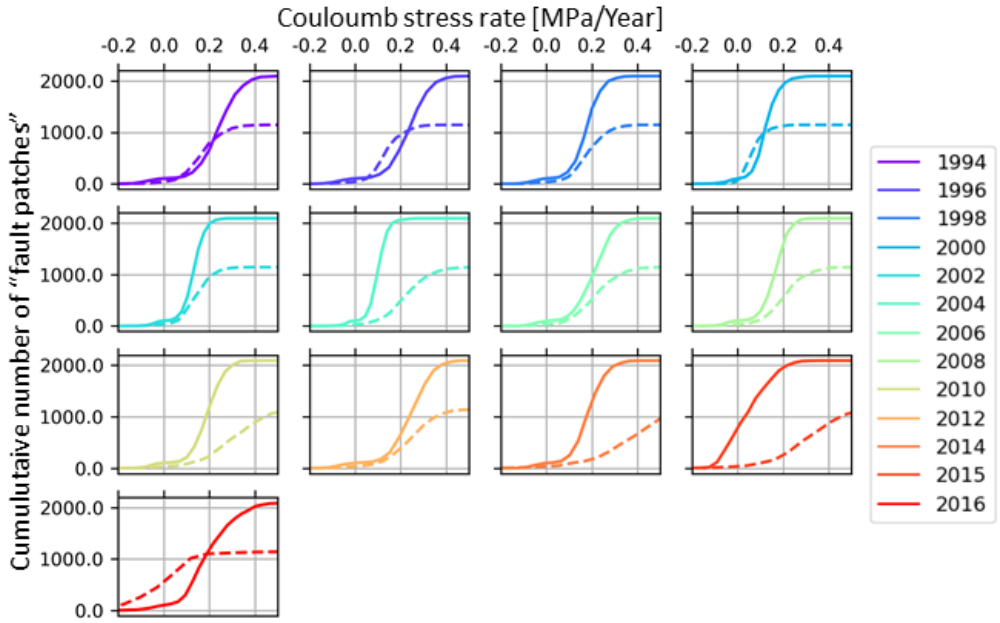

Figure 5 Cumulative distribution of the Coulomb stress rate using a Poisson's ratio of 0.2 for all the "fault patches" of both areas of interest. C-area: solid lines, SW-area: dashed lines. The large number of "fault patches" with negative stressing rates, in 2015 and 2016 for respectively the C-area and SW-area, marks the decrease of the gas production rates imposed by regulators.

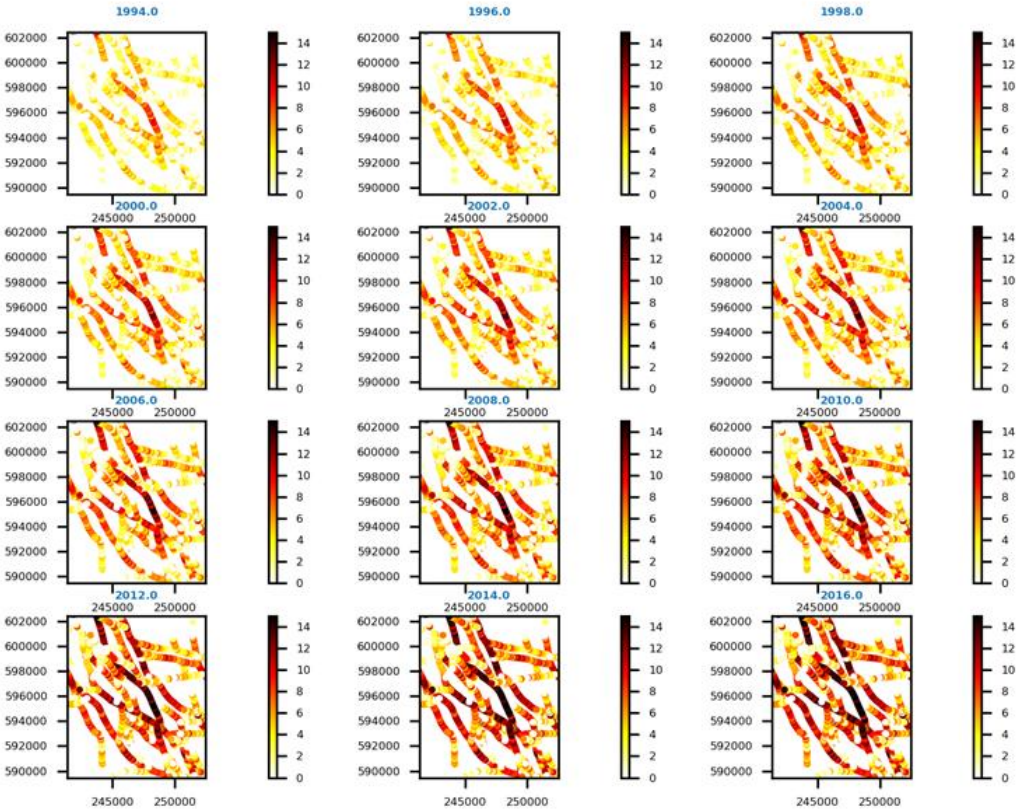

Figure 6 Spatio-temporal evolution of the Coulomb stress changes (MPa) for the C-area using a Poisson's ratio of 0.05.

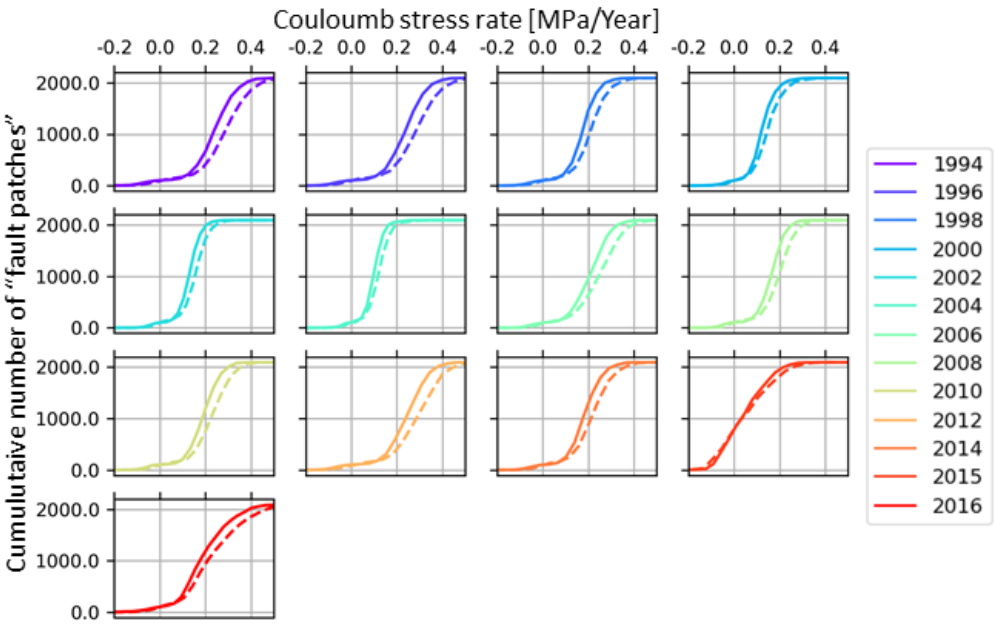

Figure 7 Cumulative distribution of the Coulomb stress rate for all the "fault patches" of the C-area, either using a Poisson's ratio of 0.2 (solid lines) or a Poisson's ratio of 0.05 (dashed lines). The large number of "fault patches" with negative stressing rates in 2015 marks the decrease of the gas production rates imposed by regulators.

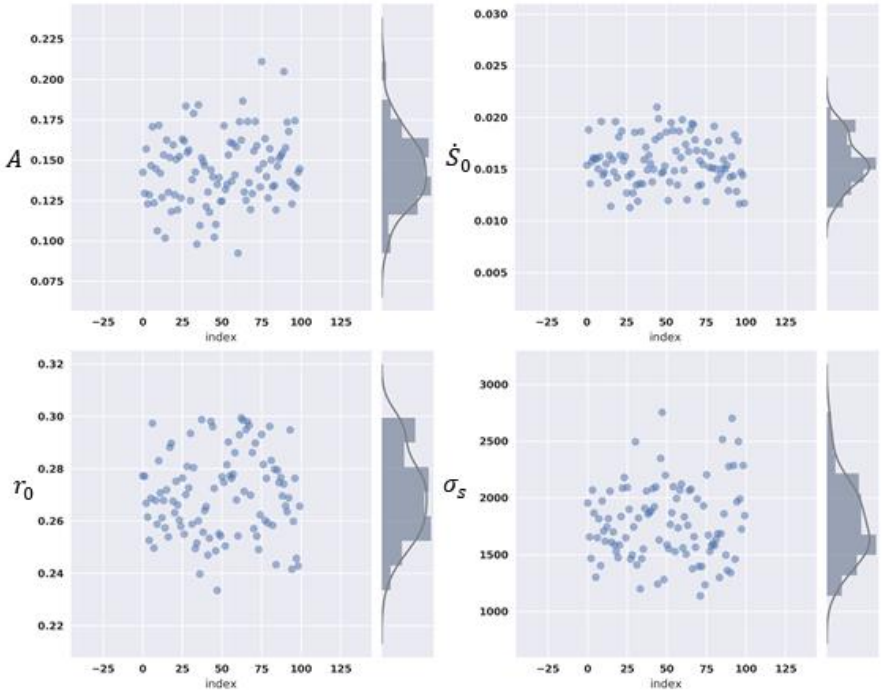

Figure 8 *Posterior probability distributions of the parameters controlling the fault frictional response (including the Gaussian smoother) for the full Groningen. Bounded uniform prior distributions for each model parameters are: A: U($1e^{-3}$, 10), $\dot{S}_0$: U($5e^{-6}$, 0.5), r_0: U($5e^{-4}$, 5), σ_s: U(500, 10000) - with U(a, b) is a uniform distribution between a and b.*

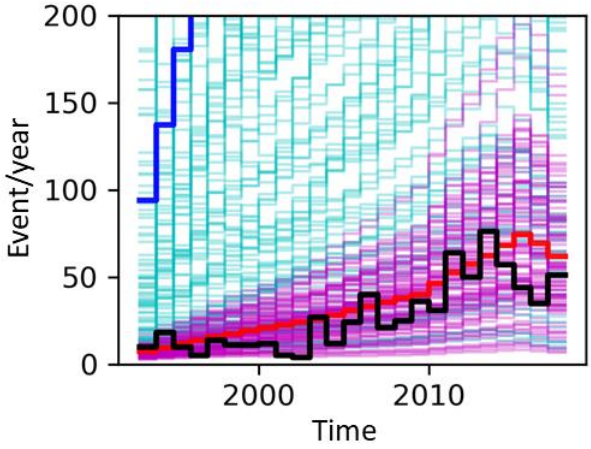

Figure 9 Comparison of the predicted seismicity histories (yearly event rate) with the data (dark) for the full Groningen. Cyan thin lines: prior ensemble with mean (thick blue line). Magenta thin lines: posterior ensemble with mean (thick red line).

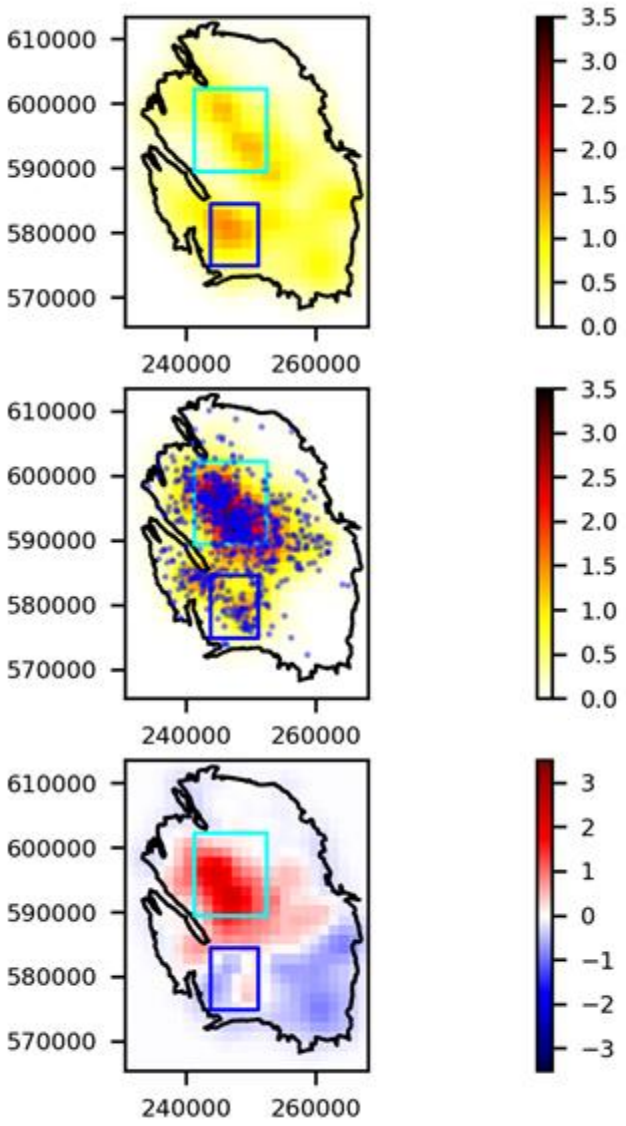

Figure 10 Comparison of the spatial pattern of the models and data event density (events per km^2) for the full Groningen and for the calibration time period [1993-2018]. Top: model, middle: data, bottom: residue. The residual map is the difference between data and model.

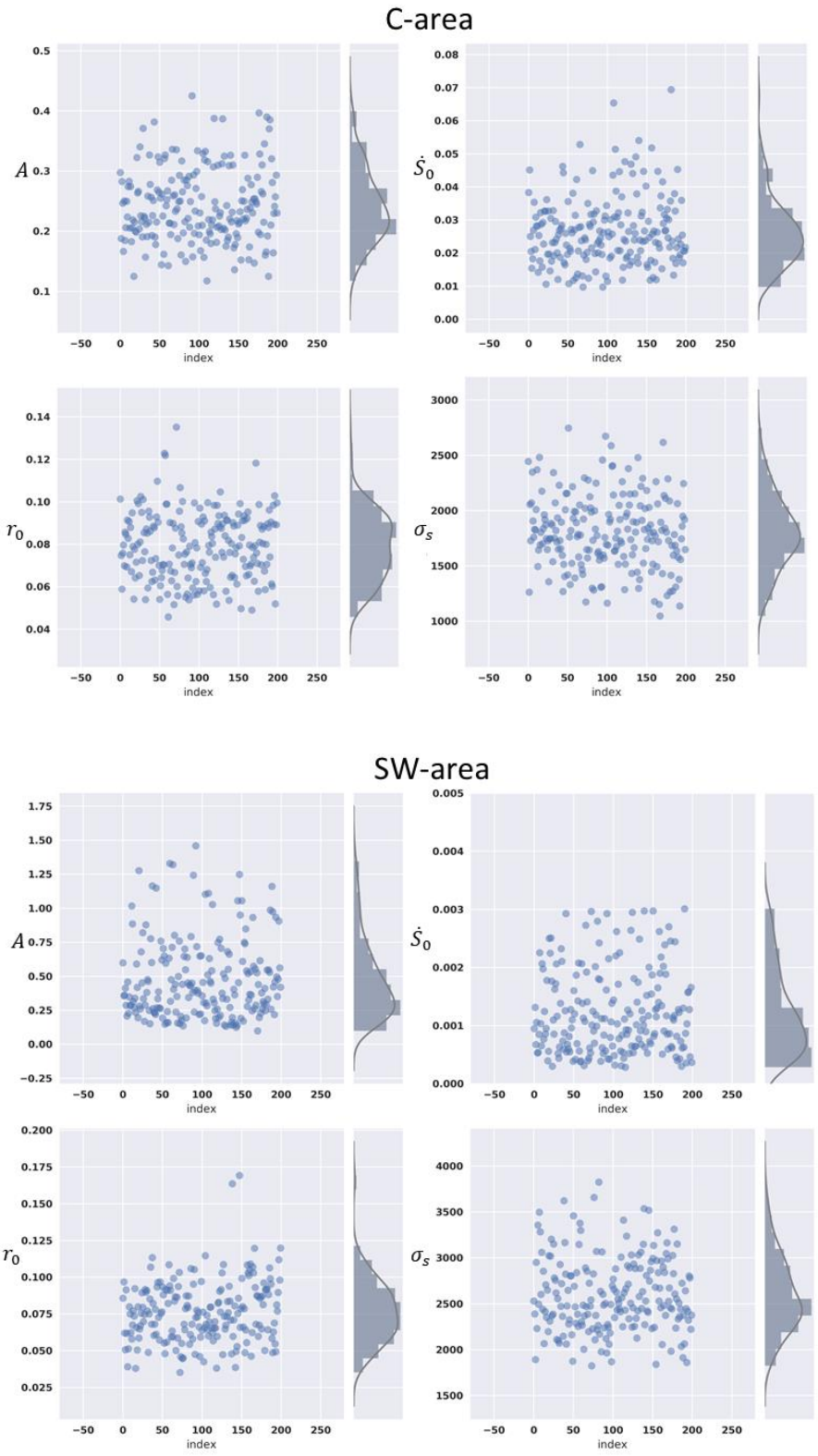

Figure 11 Posterior probability distributions of the parameters controlling the fault frictional response (including the Gaussian smoother) for both the C-area (up) and SW-area (down). Bounded uniform prior distributions for each model parameters are: A: U($1e^{-3}$, 10), $\dot{S}_0$: U($5e^{-6}$, 0.5), r_0: U($5e^{-4}$, 5), σ_s: U(500, 4500) - with U(a, b) is a uniform distribution between a and b.

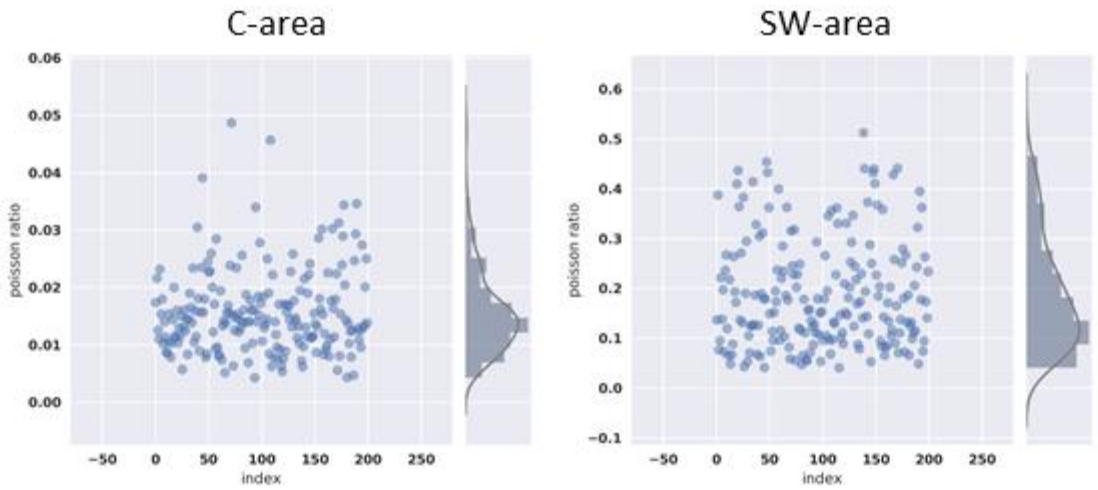

Figure 12 Posterior probability distributions of the Poisson's ratio (controlling the induced stress development) for both the C-area (left) and SW-area (right). The bounded uniform prior distribution is: ν: U(0.01, 0.5) - with U(a, b) is a uniform distribution between a and b.

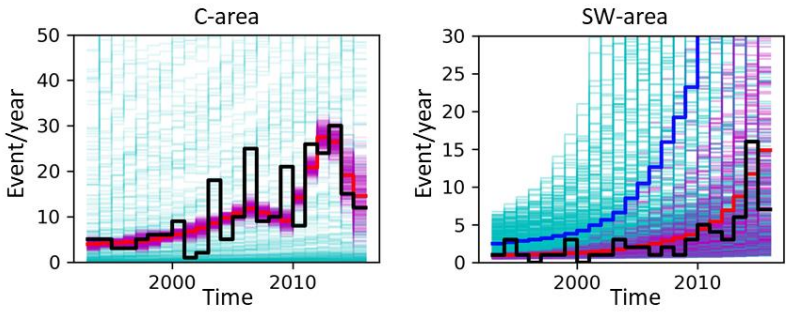

Figure 13 Comparison of the predicted seismicity histories (yearly event rate) with the data (dark) for the C-area (left) and SW-area (right). Cyan thin lines: prior ensemble with mean (thick blue line); note that the mean prior for the C-area is outside the vertical axis-range. Magenta thin lines: posterior ensemble with mean (thick red line).

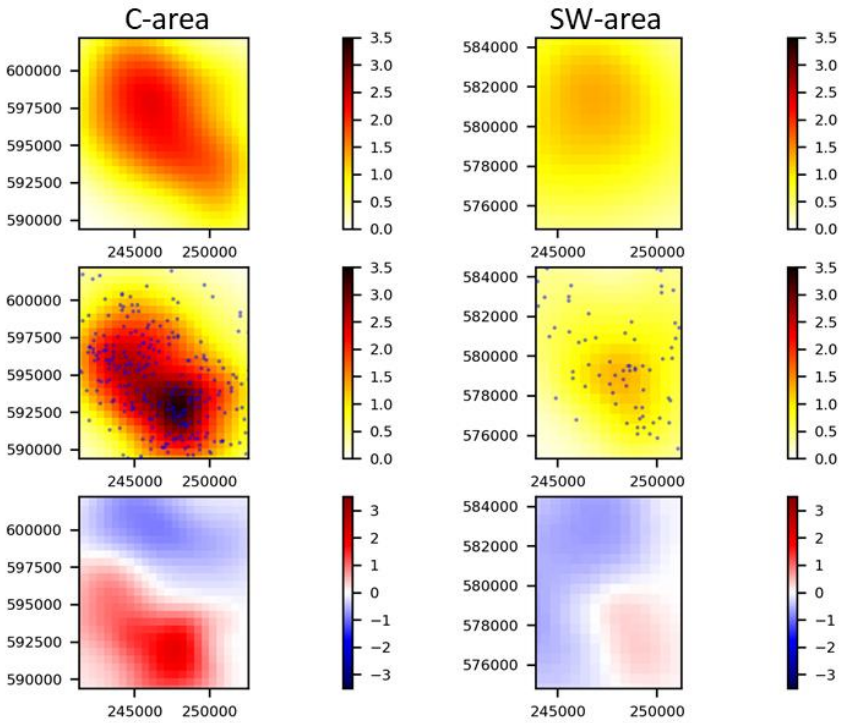

Figure 14 Comparison of the spatial pattern of the models and data event density (events per km^2) for the C-area (left) and SW-area (right) and for the calibration time period [1993-2016]. Top: model, middle: data, bottom: residue. The residual map is the difference between data and model.

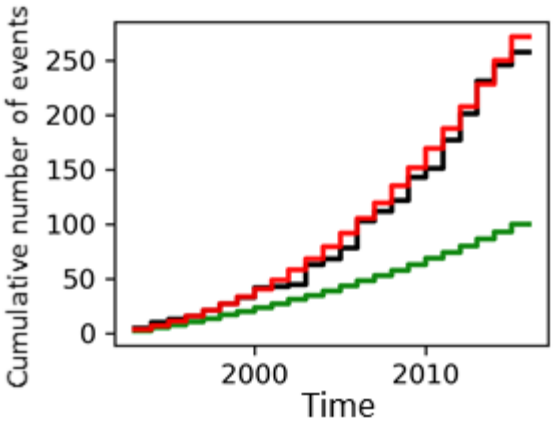

Figure 15 Joint effect of contrasted stress development and fault frictional response on the temporal evolutions of the cumulative number of events. Dark: data for the C-area. Red: model of the C-area using posterior parameters of the C-area. Green: model of the C-area using posterior parameters of the SW-area.

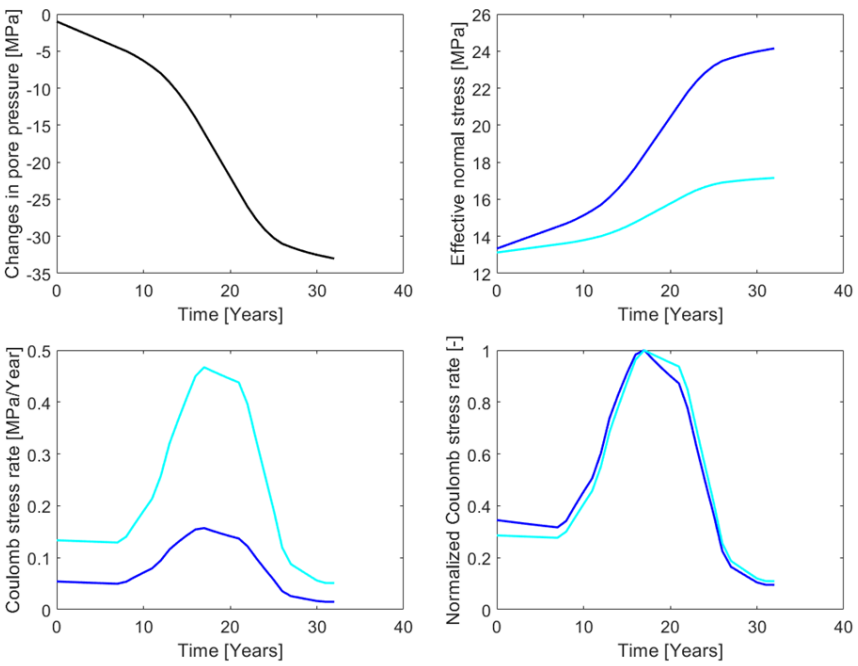

Figure 16 Effective normal stress and Coulomb stress rate histories for two different Poisson's ratio (blue curves: $\nu = 0.2$; cyan curves: $\nu = 0.05$) computed with the analytical solution of a fault (with zero offset and a dip of $70°$) embedded in a laterally extensive reservoir undergoing uniaxial compaction (Fjaer et al., 2008). Top left: depletion history representative for Groningen. Top right: effective normal stress. Bottom left: Coulomb stress rate. Bottom right: Normalized Coulomb stress rate, that is the Coulomb stress divided by its max value.

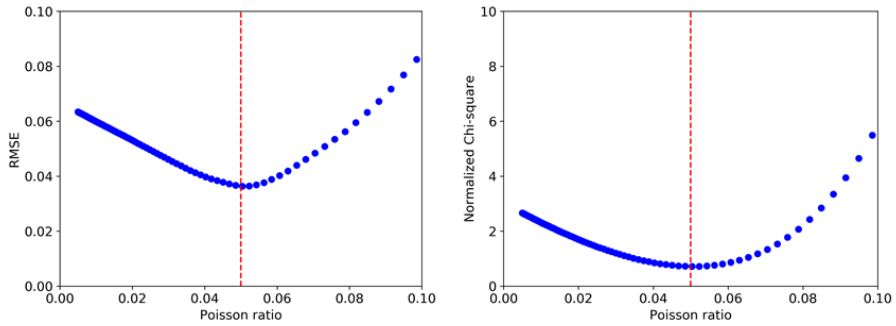

Figure 17 Distribution of the performance metrics (left: RMSE and right: $\frac{\chi^2}{N_d}$) as a function of the Poisson's ratio for the analytical exercise. The vertical dashed red lines indicate the Poisson's ratio of 0.05 used for the analytical exercise.

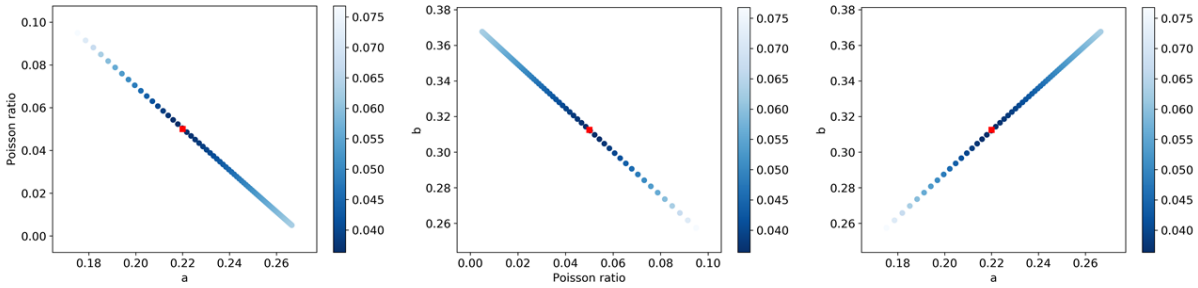

Figure 18 Covariances between the Poisson's ratio and the Dieterich's model parameters for the analytical exercise. The colorbars display the RMSE values. The red squares indicate the model parameters used for the data of the analytical exercise.

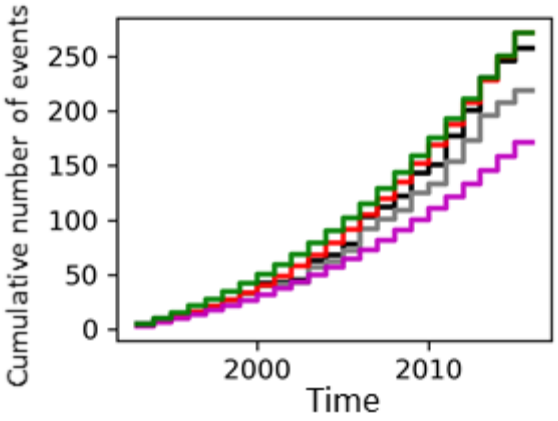

Figure 19 Effect of the Poisson's ratio and elastic stress transfers on the temporal evolutions of the cumulative number of events. Dark: data for the C-area. Grey: declustered data for the C-area. Red: model for the C-area using posterior model parameters of the C-area. Green: model for the C-area using model parameters inverted by Candela et al. (2019). Magenta: model for the C-area using model parameters of the C-area except that the Poisson's ratio is fixed at 0.2.

REFERENCES

Baù, D., Ferronato, M., Gambolati, G., Teatini, P., & Alzraiee, A. (2015). Ensemble smoothing of land subsidence measurements for reservoir geomechanical characterization. *International Journal for Numerical and Analytical Methods in Geomechanics, 39(2), 207-228.*

Bierman. S., Kraaijeveld, F., and Bourne, S. (2015). Regularised direct inversion to compaction in the Groningen reservoir using measurements from optical leveling campaigns. *Technical Report. Shell Global Solutions International. Amsterdam*.

Bourne, S.J., Oates, S.J., van Elk, J., and Doornhof, D. (2014). A seismological model for earthquakes induced by fluid extraction from a subsurface reservoir, J*. geophys. Res., 119(12), doi:10.1002/2014JB011663*.

Bourne, S.J., and Oates, S.J. (2017). Extreme threshold failures within a heterogeneous elastic thin-sheet and the spatial-temporal development of induced seismicity within the Groningen gas field, J*. geophys. Res., 122, 10 299–10 320.*

Bourne, S.J., S.J. Oates, and J. van Elk. (2018). The exponential rise of induced seismicity with increasing stress levels in the Groningen gas field and its implications for controlling seismic risk. *Geophys. J. Int. (2018) 213, 1693–1700.*

Buijze, L. (2020). Numerical and experimental simulation of fault reactivation and earthquake rupture applied to induced seismicity in the Groningen gas field. *PhD thesis.*

Candela, T., Osinga, S., Ampuero, J.-P., Wassing, B., Pluymaekers, M., Fokker, P. A., et al. (2019). Depletion-induced seismicity at the Groningen gas field: Coulomb rate-and-state models including differential compaction effect. *Journal of Geophysical Research: Solid Earth, 124, 7081– 7104. https://doi.org/10.1029/2018JB016670*

Dempsey, D., and Suckale, J. (2017). Physics-based forecasting of induced seismicity at Groningen gas field, the Netherlands, *Geophys. Res. Lett., 44, 7773-7782.*

Dieterich, J.H. (1994). A constitutive law for rate of earthquake production and its application to earthquake clustering, *Journal of Geophysical Research, 99, 2601.*

Emerick, A. A., & Reynolds, A. C. (2013a). Ensemble smoother with multiple data assimilation. *Computers & Geosciences, 55, 3-15.*

Emerick, A. A., & Reynolds, A. C. (2013b). Investigation of the sampling performance of ensemblebased methods with a simple reservoir model. *Computational Geosciences, 17(2), 325-350.*

Evensen, G. (2009). Data Assimilation: The Ensemble Kalman Filter. *Springer-Verlag Berlin Heidelberg, 10.1007/978-3-642-03711-5.*

Fjaer, E., Holt, R. M., Horsrud, P., Raaen, A. M., & Risnes, R. (2008). Petroleum related rock mechanics (2nd ed.). *Amsterdam and Oxford: Elsevier.*

Fokker P.A. and K. Van Thienen-Visser (2016). Inversion of double-difference measurements from optical leveling for the Groningen gas field. *International Journal of Applied Earth Observation and Geoinformation 49 (2016) 1–9.*

Fokker, P. A., Visser, K., Peters, E., Kunakbayeva, G., & Muntendam-Bos, A. G. (2012). Inversion of surface subsidence data to quantify reservoir compartmentalization: A field study. *Journal of Petroleum Science and Engineering, 96, 10-21.*

Fokker, P. A., Wassing, B. B. T., Van Leijen, F. J., Hanssen, R. F., & Nieuwland, D. A. (2016). Application of an ensemble smoother with multiple data assimilation to the Bergermeer gas field, using PS-InSAR. *Geomechanics for Energy and the Environment, 5, 16-28.*

Foreman-Mackey, D., D. W. Hogg, D. Lang, and J. Goodman (2013). emcee: The MCMC hammer, *Publ. Astron. Soc. Pac., 125 (925), 306.*

Heimisson, E. R., J. D. Smith, J-P. Avouac (2020). Modeling Induced Seismicity on Dormant Faults: Application to the Groningen Gas field. *AGU Fall Meeting 2020.*

Hol, S., Mossop, A., van der Linden, A., Zuiderwijk, P. M. M., & Makurat, A. (2015). Long-term compaction behavior of Permian sandstones - An investigation into the mechanisms of subsidence in the Dutch Wadden Sea. *49th US Rock Mechanics / Geomechanics Symposium, ARMA 15-6184, 1-8.*

Hol, S., van der Linden, A., Bierman, S., Marcelis, F., & Makurat, A. (2018). Rock physical controls on production-induced compaction in the Groningen Field. *Scientific Reports, 8 (1), 7156.*

Menke, W. (1989). International Geophysics Series. Geophysical data analysis: Discrete inverse theory, 45.

Nederlandse Aardolie Maatschappij (NAM) (2016). Technical Addendum to the Winningsplan Groningen 2016; Production, Subsidence, Induced Earthquakes and Seismic Hazard and Risk Assessment in the Groningen Field., 57 pp, available at http://www.nam.nl/algemeen/mediatheek-en-downloads/winningsplan-2016.html.

Pijnenburg, R. P. J., Verberne, B. A., Hangx, S. J. T., & Spiers, C. J. (2018). Deformation Behavior of Sandstones From the Seismogenic Groningen Gas Field: Role of Inelastic Versus Elastic Mechanisms. *Journal of Geophysical Research: Solid Earth, 123 (7), 5532-5558.*

Pijnenburg, R. P. J., Hangx, S. J. T., & Spiers, C. J. (2019). Inelastic deformation of the Slochteren sandstone: Stress-strain relations and implications for induced seismicity in the Groningen gas field. *Journal of Geophysical Research: Solid Earth, 124 (5), 5254-5282.*

Rubin AM. and J.P. Ampuero (2007). Aftershock asymmetry on a bimaterial interface, *J. Geophys. Res., 112, B05307, doi:10.1029/2006JB004337.*

Segall, P. & Fitzgerald, S.D. (1998). A note on induced stress changes in hydrocarbon and geothermal reservoirs, *Tectonophysics, 289, 117.*

Segall, P., and S. Lu (2015). Injection-induced seismicity: Poroelastic and earthquake nucleation effects, *J. Geophys. Res. Solid Earth, 120, 5082–5103, doi:10.1002/2015JB012060.*

Smith, J. D., Avouac, J.-P., White, R. S., Copley, A., Gualandi, A., & Bourne, S. (2019). Reconciling the long-term relationship between reservoir pore pressure depletion and compaction in the Groningen region. *Journal of Geophysical Research: Solid Earth*, 124, 6165– 6178. https://doi.org/10.1029/2018JB016801

Tarantola, A. (2005). Inverse problem theory and methods for model parameter estimation (Vol. 89). SIAM.

Tarrahi, M., and Jafarpour, B. (2012), Inference of permeability distribution from injection-induced discrete microseismic events with kernel density estimation and ensemble Kalman filter, *Water Resour. Res., 48, W10506, doi:10.1029/2012WR011920.*

Tarrahi, M., Jafarpour, B., and Ghassemi, A. (2015), Integration of microseismic monitoring data into coupled flow and geomechanical models with ensemble Kalman filter, *Water Resour. Res., 51, 5177– 5197, doi:10.1002/2014WR016264.*

Van Leeuwen, P.J., & Evensen, G. (1996). Data Assimilation and Inverse Methods in Terms of a Probabilistic Formulation, *Monthly Weather Review, 124(12), 2898-2913.*

van Wees J.D., S. Osinga, K. Van Thienen-Visser, and P.A. Fokker (2018). Reservoir creep and induced seismicity: inferences from geomechanical modeling of gas depletion in the Groningen field, *Geophysical Journal International, 212, 1487-1497.*

van Wees J.D., Maarten Pluymaekers, Sander Osinga, Peter Fokker, Karin Van Thienen-Visser, Bogdan Orlic, Brecht Wassing, Dries Hegen, Thibault Candela, 3-D mechanical analysis of complex reservoirs: a novel mesh-free approach, *Geophysical Journal International*, Volume 219, Issue 2, November 2019, Pages 1118–1130, https://doi.org/10.1093/gji/ggz352

Zaliapin, I., A. Gabrielov, V. Keilis-Borok, and H. Wong (2008). Clustering analysis of seismicity and aftershock identification. *Phys. Rev. Lett., 101, 018501. doi: 10.1103/PhysRevLett.101.018501.*

Zaliapin, I. and Y. Ben-Zion (2013). Earthquake clusters in southern California, I: Identification and stability. *J. Geophys. Res., 118, doi: 10.1002/jgrb.50179.*

Zaliapin, I. and Y. Ben-Zion (2016). Discriminating characteristics of tectonic and human-induced seismicity. *Bull. Seismol. Soc. Am., 106(3), 846-859, doi: 10.1785/0120150211.*

Zhai, G., M Shirzaei, M Manga, X Chen. 2019. Pore-pressure diffusion, enhanced by poroelastic stresses, controls induced seismicity in Oklahoma. *Proceedings of the National Academy of Sciences 116 (33), 16228-16233.*

ACKNOWLEDGEMENTS

The earthquake catalogue used for this study can be found at the KNMI website at www.knmi.nl.